Astron. Astrophys. 364, 859–872 (2000)

ASTRONOMY AND ASTROPHYSICS

Location of the source of soft X-ray non-thermal line broadenings in a solar flare

N.D.R. Ranns, S.A. Matthews, L.K. Harra, and J.L. Culhane

University College London, Mullard Space Science Laboratory, Holmbury St. Mary, Dorking, Surrey, RH5 6NT, UK

Received 17 July 2000 / Accepted 25 October 2000

Abstract. We determine the location of the source of the non-thermal Soft X-ray line broadenings in an M1.7 two-ribbon solar flare using multi-wavelength observations. Using a combination of the Yohkoh Soft X-ray Telescope (SXT), Hard X-ray Telescope (HXT), Bragg Crystal Spectrometer (BCS) and the Transition Region and Coronal Explorer (TRACE), we find the source of the non-thermal broadenings, at their peak value, to be located in and above the SXR flare loops, not at the flare loop footpoints. After eliminating the footpoints as a potential source we discuss the likelihood that the source of non-thermally broadened emission lines is either evaporating chromospheric plasma or plasma above the Soft X-ray flare loop that is associated with the flare energy release.

Key words: Sun: flares – Sun: X-rays, gamma rays

1. Introduction

There has been much previous work on solar flares that has centered around the understanding of the observed non-thermal broadening of soft X-ray (SXR) emission lines. The non-thermal broadening is defined as the difference between the Doppler temperature (T_d) and the plasma temperature (T_e). In an ionized He -like species these temperatures are derived from the width of the main resonance line and the ratio of the main resonance line and the satellite lines respectively. This temperature difference is often expressed as a non-thermal velocity (V_{nt}) where;

$$V_{nt} = \sqrt{\frac{2k(T_d - T_e)}{m_i}}, \quad (1)$$

where k is the Boltzmann constant and m_i the mass of the ion under consideration.

Studies of V_{nt} characteristics have been carried out by a number of spaced based instruments, including Skylab, P78-1 and the Solar Maximum Mission (SMM). Results from these studies (e.g. Doschek et al. 1986) showed that they can be approximated as Gaussian broadening with peak values ranging from $150kms^{-1}$ to $300kms^{-1}$. They are present before the peak of the hard X-ray (HXR) flux and diminish to between $0kms^{-1}$ and $50kms^{-1}$ by the time of SXR maximum. There is no correlation observed between maximum V_{nt} and position on the disk. There is also evidence for the presence of V_{nt} in C IV ($T_{max} = 1 \times 10^5 K$) spectral lines at $\approx 50kms^{-1}$.

In a large study of small flares Harra-Murnion et al. (1997) examined the variation of V_{nt} with electron temperature, GOES classification, duration of event, rise time and source size of the SXR event. Their results showed that V_{nt} is independent of flare size, complexity and intensity of hard X-ray (HXR) bursts, but there is a weak dependence on duration and rise time. The longer the rise time the lower the value of V_{nt} and there is a trend of increasing V_{nt} with ele ctron temperature.

However, the nature and location of the source of the non-thermal broadenings is still unknown as indeed is its role in the flare process. For example, are they a direct signature of the flare energy release process, or a hydrodynamic response of the solar atmosphere to the injection of flare energy? Fig. 1 shows a schematic diagram of a proposed unified flare model (Shibata 1999). Within this single loop flare model there exist five plausible locations where the source of V_{nt} could be located. These five regions are numbered on Fig. 1 and are described below.

1) The Reconnection Site: At the site of magnetic field line reconnection and possible particle acceleration, the density must be small to allow for efficient particle acceleration (Miller et al. 1997) and will have very small spatial scales. Thus the emission measure is likely to be low. New evidence for the presence of inflows to the reconnection region has recently been presented (Yokoyama 2000), however the reconnection region itself remains unresolved. Hence this region is an unlikely source of the observed V_{nt}.
2) The above the loop HXR source: The nature of the HXR above the loop top source is still a topic of considerable debate (Fletcher 1999; Somov 1999). The two most popular explanations for the creation of HXRs above the loops are from a super-hot source ($\approx 100MK$) generated by the fast shock (Masuda 1994; Tsuneta et al. 1997; Tsuneta & Naito 1998) or from thin-thick target Bremsstrahlung from trapped electrons (Wheatland & Melrose 1995; Fletcher & Martens 1998; Metcalf & Alexander 1999). This above the

Send offprint requests to: N.D.R. Ranns
Correspondence to: ndrr@mssl.ucl.ac.uk

loop source is believed to be confined by two slow mode shocks that extend down from the reconnection region (not shown in Fig. 1) and confine the energetic electrons by acting as magnetic mirrors (Tsuneta & Naito 1998). Very hot SXR plasma has also been observed to originate from above the loop top and is believed to be heated by the slow shocks (Tsuneta 1996; Tsuneta et al. 1997)

3) The SXR loop top: Unusually bright loop tops have been reported by Doschek & Feldman (1996) using SXT, the presence of which can be explained by the model of Jakimiec et al. (1998) which invokes a turbulent loop-top kernel within which the magnetic field is tangled and transient current sheets occur.
4) Evaporating chromospheric plasma: This is a direct consequence of the flare electron deposition at the footpoints, initiated when the energy deposition rate greatly exceeds the rate at which the energy can be conducted and radiated away. The plasma expands explosively and is driven up the magnetic loop into the corona by strong induced pressure gradients.
5) Flare loop footpoints: Visible at HXR, chromospheric and transition region wavelengths, these result from the deposition of flare electrons in the chromosphere at the base of the magnetic loop, where they produce HXRs via thick target Bremsstrahlung and supply heat to the chromosphere.

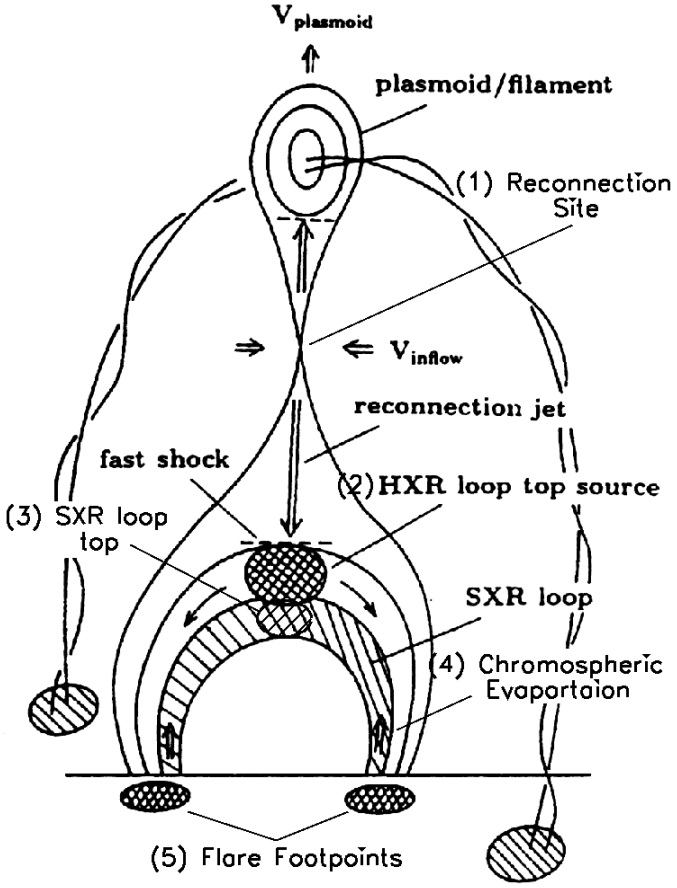

Fig. 1. A schematic diagram of a unified model of solar flares. From Shibata (1999).

The regions described above are created by a variety of different processes associated with a flare. By eliminating regions that are not responsible for producing the observed non-thermal broadenings and ultimately locating the region(s) of the flare that are responsible, we can eliminate and identify possible mechanisms responsible for the generation of V_{nt}.

In order to distinguish between these possibilities, studies of occulted limb flares, in which the flare footpoints are obscured by the solar disk, have been undertaken (Khan et al. 1995; Mariska et al. 1996; Mariska & McTiernan 1999). Khan et al. (1995) and Mariska & McTiernan (1999) showed that for partially occulted limb flares the measured V_{nt} was similar to that observed for disk flares, indicating that the source of the V_{nt} could not be the flare footpoints since these were occulted by the limb. Khan et al. (1995) concluded that the source of the V_{nt} was at the loop top or that V_{nt} is the same throughout the loop. These results are contradictory to those of Mariska et al. (1996) who, using a smaller data set, showed a tendency for occulted flares to have a lower V_{nt}.

Doschek et al. (1986) and Mewe et al. (1985) have suggested that the observed V_{nt} can be explained by the fact that full Sun Bragg crystal spectrometers observe an integrated spectrum of plasma moving at a range of velocities. Fludra et al. (1989) showed a weak correlation between V_{nt} and the measured blue shift velocity and Mariska et al. (1993) showed a correlation between line width and the line centroid shift. These results indicate that chromospheric evaporation could account for at least some of the observed V_{nt} particularly after the flare impulsive phase.

Recent work by Ding et al. (1999) using 2D spectra of a resolved flare loop has shown that the $H\alpha$ profiles are more broadened at the loop top than anywhere else along the loop. However, although the $H\alpha$ loops are believed to cool from SXR loops, this result should not be taken as true for SXR loops as well since flare loops in Hα are often only seen when the SXR non-thermal broadenings have decayed.

Knowledge of how the values of V_{nt} develop over time can also place stringent criteria on the location and generation of the V_{nt}. Alexander et al. (1998) studied the relationship between the peak times in V_{nt} and the HXR flux and showed that the peak of the V_{nt} occurred before the maximum in hard X-rays. Mariska & McTiernan (1999) in a similar study of a larger sample observed that, for the majority of the events they studied, the peak in V_{nt} occurs after the first significant HXR peak, although the opposite behaviour was seen in a minority of events. The attainment of high values of V_{nt} early in a flare, a similar result from both studies, is more indicative of plasma turbulence rather than hydrodynamic flows as the source of V_{nt} (Alexander et al. 1998).

The aim of this paper is to determine the location of the non-thermal broadenings seen in the *Yohkoh* BCS Ca XIX channel. By determining the location of the source of V_{nt} it will be possible to eliminate some probable V_{nt} generation mech-

Table 1. Temperature of maximum formation (T_{max}) and the detector wavelength ranges (λ_r) that cover the BCS ions.

Ion	$\log T_{max}$	λ_r
S XV	$6.8 \rightarrow 6.9$	$5.016 \rightarrow 5.114$
Ca XIX	$7.1 \rightarrow 7.2$	$3.163 \rightarrow 3.191$
Fe XXV	7.6	$1.830 \rightarrow 1.894$
Fe XXVI	$8.0 \rightarrow 8.1$	$1.764 \rightarrow 1.804$

anisms and possibly determine their role in the flare process. To accomplish this goal we use multi-wavelength data from the SXT, BCS, HXT instruments on *Yohkoh* in conjunction with TRACE. In Sect. 2 we outline the instrumentation used in this study and in Sect. 3 describe the basic properties of the studied flare. In Sect. 4 we describe the method used to locate source of the V_{nt} and present our results which eliminate the footpoints as the source of V_{nt}. In Sect. 5 we discuss the implications of our results and probable locations for the source of V_{nt}.

2. Instrumentation

The Bragg Crystal Spectrometer on board *Yohkoh* (BCS, Culhane et al. 1991; Lang et al. 1993) is a full Sun instrument. It uses four bent crystals to observe simultaneously the spectrum of soft X-ray lines in four narrow wavelength ranges centered around the principle resonance lines of He-like S XV, Ca XIX, Fe XXV and H-like Fe XXVI. Temperature of maximum formation and the detector wavelength ranges (λ_r) that cover the BCS ions are shown in Table 1. Temperatures of maximum formation (T_{max}) are taken from Arnaud & Rothenflug (1985) throughout this article. In this paper we examine only the Ca XIX data. The S XV data were unfortunately contaminated by the many active regions on the disk, hence the spectra in the early phases of the flare showed two distinct components. Ca XIX data was used in preference to the iron lines because it is closer in temperature to the response of SXT.

The Soft X-ray Telescope (SXT, Tsuneta et al. 1991) is a grazing incidence X-ray telescope operating in the wavelength range 2→70Å. Plasma diagnostics are achieved by formulating the ratios of images taken with various broad band filters which have different signal responses at different temperatures. In flare mode SXT takes a full resolution image in each filter every two seconds and cycles through the four different filters. The spatial resolution is 5 arc-seconds (pixel size 2.5 arc-seconds).

The Hard X-ray Telescope (HXT, Kosugi et al. 1991) is a Fourier synthesis imager of 64 elements and 4 energy channels which operate in the range $14keV$ to $93keV$. Each subcollimator measures a spatially-modulated incident photon count, which is Fourier-transformed into an image. During flare mode the temporal resolution is 0.5 seconds.

The Transition Region and Coronal Explorer (TRACE, Handy et al. 1999; Schrijver et al. 1999) employs multi-wavelength optics and a lumogen coated CCD to record three EUV wavelengths and several UV wavelengths. TRACE views plasma at selected temperatures from $6000K$ to $10MK$ with a maximum field of view of 8.5 arc-minutes square, spatial resolution of 1 arc-second (0.5 arc-second pixels) and a typical temporal resolution of less than a minute. For this flare study the TRACE was observing with all of its EUV filters, namely 171 Å(Fe IX, $\log T_{max} = 5.9 \rightarrow 60$), 195 Å(Fe XII, $\log T_{max} = 6.2$) and 284 Å(Fe XV, $\log T_{max} = 6.3$) and with the Lyman α (Lα) filter at 1216 Å. The cadence in the EUV images was typically 160 seconds with approximately 6 seconds exposure times. The cadence at Lα was typically 30 seconds with 0.7 second exposures. TRACE observations of the flaring active region began at 18:00UT and continued for several hours.

3. Flare properties and evolution

The flare was a GOES M1.7 class event which occurred in NOAA Active Region 8592 (N20E40) on the 22^{nd} June 1999 as part of the first Max Millennium observing campaign. The GOES start time was approximately 18:15UT with a maximum at 18:29UT in the 1 to 8 Å channel.

In the pre-flare stages Big Bear Solar Observatory (BBSO) Hα images show the ejection of a filament beginning at 18:10UT. After 18:10UT the filament can be seen in emission in all TRACE filters, indicating that the structure is multi-thermal. A Coronal Mass Ejection (CME) was also observed by the Large Angle Spectroscopic Coronograph (LASCO) ejected from the North-East quadrant. The calculated onset time of the CME, from its velocity profile, was 18:00UT to within an hour. During the filament eruption SXT was observing a different active region in which a GOES C2.6 class event was decaying and within which a small brightening occurred. An SXT and GOES temperature analysis of these events revealed that we cannot reliably discount Ca XIX emission originating from these events. Therefore the BCS data before 18:20UT, the start of the studied M-class event, has two possible sources and hence cannot be utilized fully. SXT began observing AR8592 at 18:20:30UT when flare mode was triggered.

The flare displays two footpoint regions that outline the bases of the flare arcade and are visible in HXR and TRACE images (Fig. 2). The footpoints are located on either side of a simple photospheric magnetic neutral line (Fig. 2a). These footpoints are observed (in Lα) to move apart, away from the neutral line, as the flare progresses. Both footpoint areas are elongated in shape with the longer axis parallel to the neutral line (Fig. 2b). The suth footpoint area exhibits stronger emission at both Lα and HXR wavelengths, indicating greater energy deposition. The magnetic field strength at the south footpoint is weaker than the north footpoint, in agreement with the results of Sakao (1994). He found that greater electron deposition occurs at the magnetically weaker (south) footpoint due to reduced mirror forces experienced by the electrons propagating along the magnetic field.

HXT images of the impulsive phase show two footpoints, one on either side of the photospheric neutral line. These footpoints are visible in the LO(14-23keV; Fig. 2(e)), M1(23-33keV; Fig. 2f) and M2(33-53keV) channels. T HI(53-93keV) channel does not contain enough counts to formulate an image. Images in the low channel also show a HXR source located above the

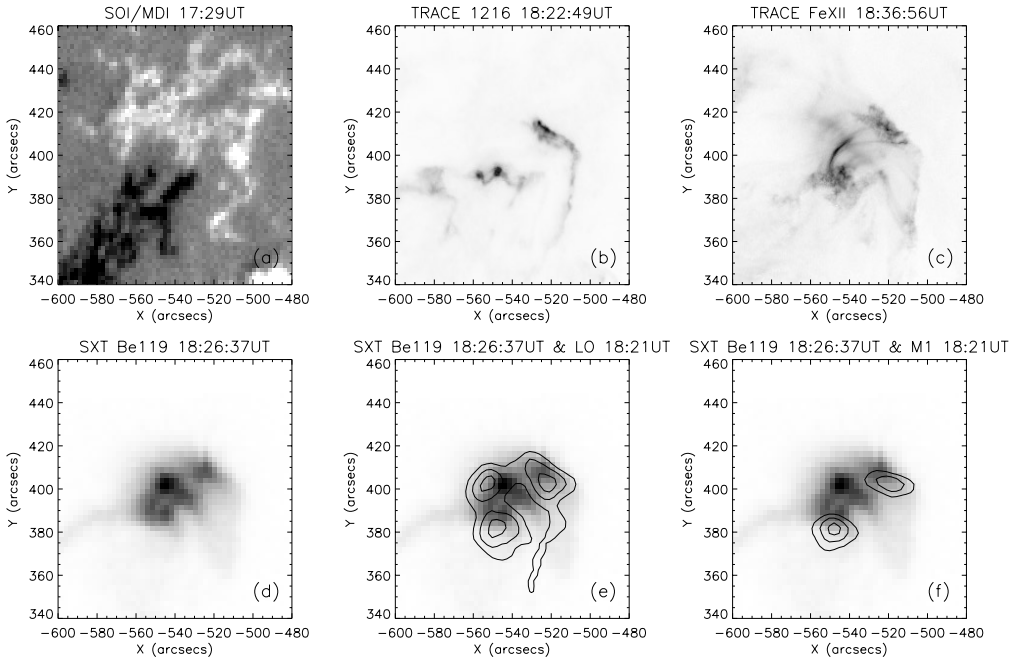

Fig. 2a–f. Images of the studied flare: **a** MDI magnetogram, **b** TRACE Lymanα, **c** TRACE Fe XII/Fe XXIV, **d** SXT Be119 **e** HXT LO channel and **f** HXT M1 channel. Spatial co-ordinates in this figure and throughout are arcseconds from Sun centre.

SXR loops, slightly offset to the south from the loop apex. This source is not present in the higher energy cha nnels so no diagnostics are possible. The lack of counts in the higher energy channels suggests this loop source is thermal. Unfortunately there are too few images to create reliable lightcurve comparisons with the footpoint sources. The double footpoint and loop top source are only visible from 18:21→18:23UT, the time at which the HXR flux in the LO, M1 and M2 channels was high. An arcade of flare loops connecting the two footpoints is visible first (18:24UT) at high temperatures (SXR and Fe XXIV, Fig. 2d) and then later (18:35UT) at cooler temperatures (Fe IX and Fe XII, Fig. 2c). These cool flare loops continue rising, visible in TRACE Fe XII and Fe IX lines, until at least 21:00UT. The orientation of the flare loop arcade and footpoints is such that we observe the top of the loop system against the dark background of the disk. Hence the signal from the top of the loop arcade is not contaminated by emission from the footpoints.

The combined multi-wavelength images of this flare suggest it was of the type described by Carmichael (1964), Sturrock (1966), Hirayama (1974) and Kopp & Pneuman (1976) (hereafter CSHKP) and subsequently by other authors. In this model reconnection begins low in the corona after the ejection of mass, and proceeds upwards creating a loop arcade with a temperature differential in height and footpoints that move apart with time.

4. Location of the source of V_{nt}

In this paper we examine the Ca XIX resonance line and the $n \geq 3$ satellite lines. Plasma parameters are calculated from a best fit theoretical spectrum to the observed data. Two sample BCS spectra are shown in Fig. 3 from the time of V_{nt} maximum and the maximum in BCS Ca XIX counts. The plots show that the observed data are well represented by a single component fit at both times. Two component fits to the data were attempted and although these yielded similar χ^2 values, the calculated plasma parameters were unphysical: blue shift velocities were zero and $T_d \approx 300MK$. The BCS Ca XIX lightcurve and the derived plasma parameters are shown in Fig. 4. The total count rate in the Ca XIX channel has been corrected by a dead-time factor, which varies during the flare, and has a maximum value of two. This is large and results from the large count rate in the S XV channel of ≈ 9000 Counts per second. Since the S XV and Ca XIX channels share the same detector the dead-time correction factor is calculated from the combined counts in the two channels.

Fig. 5 shows the relative timings of the non-thermal broadenings and the M1 channel HXR flux. The time of V_{nt} peak can be well determined for this event and is seen to occur after the first small HXR peak (≈18:20UT) and before t he maximum in HXRs.

We also note here that the wavelength shift of the main resonance line changes complementary to the V_{nt} throughout the flare (Fig. 4(e)). The spectral resolution of the Ca XIX detector is $0.53m$ Å, therefore the measured centroid shift is approximately two pixels ($\approx 100kms^{-1}$). If we assume that these line shifts are representative of bulk plasma motions associated with chromospheric evaporation the $100kms^{-1}$ shift places a lower limit on the up-flow velocity.

The temperature responses of the SXT filters and the BCS Ca XIX channel are shown in Fig. 6. This plot shows that although SXT is more sensitive to lower temperature plasma (i.e. $T_e < 10MK$) it also detects plasma at Ca XIX temperatures. Hence to locate the dominant source of Ca XIX emission we use images taken by SXT through the two thickest filters, Al12 and Be119.

We use the SXT to determine the spatially resolved distribution of temperature and emission measure within the flare area. When generating SXT temperature and emission measure im-

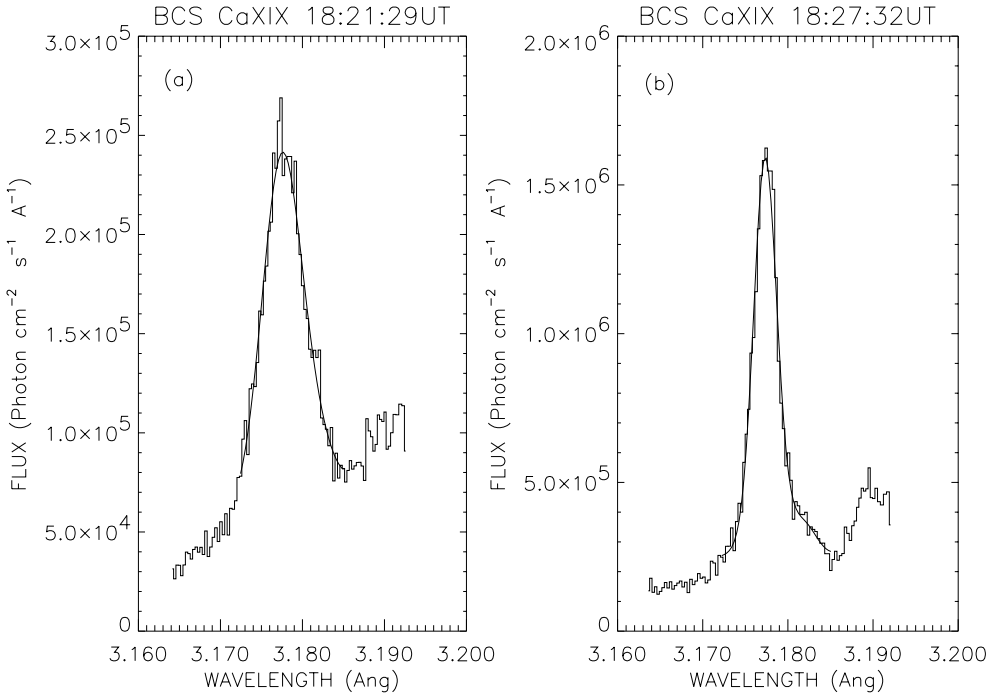

Fig. 3a and b. Two sample BCS Ca XIX spectra (histogram) and the best fitting theoretical spectrum (solid line). The times are at V_{nt} maximum (**a**) and BCS Ca XIX counts maximum (**b**).

ages the SXT images are summed over the same time range as the BCS data to improve the counting statistics. This increases the accuracy of the calculated plasma parameters and makes the values derived from both instruments directly comparable.

Fig. 7 shows temperature, emission measure and intensity images calculated from SXT from times around the V_{nt} maximum. Pixels in the SXT temperature maps that had a temperature within one standard deviation of the BCS temperature at that time were averaged to produce the derived SXT parameters. These pixels are enclosed by the contours in the SXT intensity image. The derived SXT temperatures are thus similar to that from BCS. If the emission measures from SXT are similar to that derived from BCS then we can assume that the two instruments are observing approximately the same plasma. At 18:20:47UT (Fig. 7a) the emission measures differ by less than a factor of 2 within the errors and at 18:21:29UT (Fig. 7b) the values are the same to within the errors. Thus early in the flare, around the time of V_{nt} maximum SXT and BCS are observing approximately the same plasma.

Fig. 8 shows a plot of the SXT emission measure and temperature derived this way, along with the BCS temperature and emission measure, as a function of time. The plot shows that early in the flare the derived emission measures differ only slightly and change co-temporally, but as the flare progresses the differences become more significant. The BCS emission measures are also systematically higher than the SXT emission measures. The systematic differences imply that not all the hot component is seen by SXT, some of it is superimposed along the line of sight with cooler plasma (cf. Doschek 1999). The divergence indicates that this effect becomes stronger in the later stages of the flare. Cooler plasma along the line of sight will dominate SXT's response, resulting in lower derived temperatures. Hence pixels in which the hot component may be present along with cooler plasma will not show a high temperature in SXT and will not be within one standard deviation of the BCS temperature. These pixels will not therefore contribute to the SXT derived temperature and emission measure of the hot component but will be included in the BCS derivation, hence the discrepancy. Therefore, only before 18:23:00UT can we reliably say that SXT and BCS are observing essentially the same plasma.

The hot pixels enclosed by the contours in Fig. 7a and b are spread over the whole flare area. However, the dominant emission will come from those hot pixels where the emission measure is also high. These high emission measure, high temperature pixels are located in an area extended along the flare loops above the footpoint emission.

Wülser et al. (1994) used a similar method of comparing SXT and BCS temperatures and emission measures in the early phase of a solar flare. In their analysis the derived plasma parameters from BCS and SXT differed by similar amounts to the values calculated here and led them to conclude that BCS and SXT were observing the same plasma. This enabled them to determine that the location of up-flowing SXR plasma, detected by BCS, was within a SXR flare loop connecting two HXR footpoints.

To verify our result that the BCS is detecting only the flare loop plasma and no additional sources, we compare the lightcurves of the BCS Ca XIX with the SXT pixels (DN/s, Be119 filter) that have a temperature in the range of $\log T_e = 7.1 \rightarrow 7.3$ (the range over which BCS CaXIX is most sensitive). The results are shown in Fig. 9. The fact that these two lightcurves behave similarly (in the early stages of the flare) suggests that both instruments are observing the same plasma

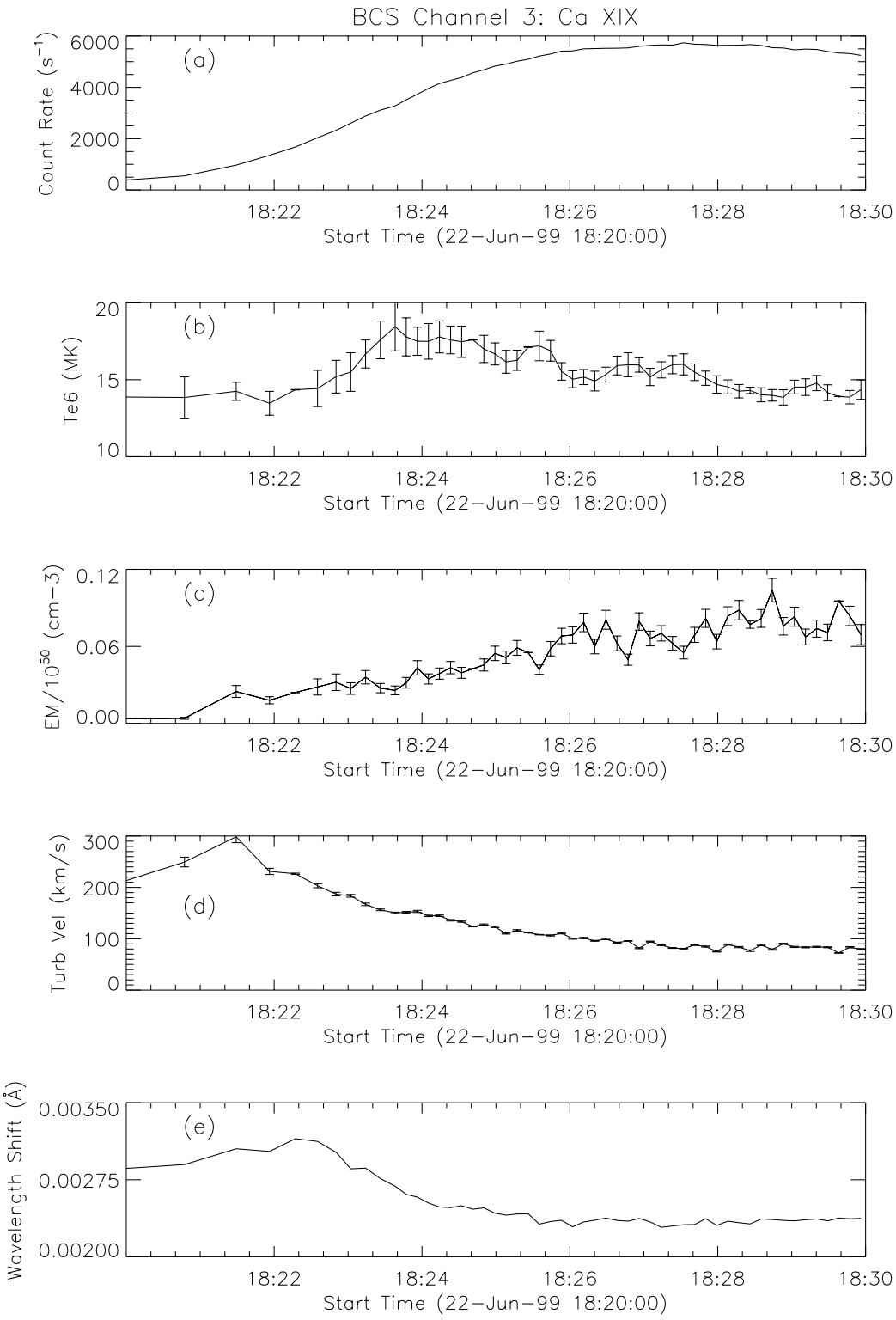

Fig. 4a–e. The results from the spectral fitting of the BCS Ca XIX data.

and that neither instrument is also detecting another source. Also shown in Fig. 9 is the lightcurve of the SXT cool component ($\log T_e = 6.6 \rightarrow 6.9$), the accumulation of this lower temperature plasma inhibits the ability of SXT to detect the hot component, hence the discrepancies between the hot component and BCS lightcurves after 18:24UT.

It is now well established that during solar flares the TRACE 195 Å image becomes considerably contaminated by emission from Fe XXIV(λ=192 Å, Feldman et al. 1999; Warren et al. 1999; Warren 2000). Fe XXIV and Ca XIX ionization fraction functions both peak at the same temperature (Arnaud & Rothenflug 1985), therefore emission in these two spectral lines should

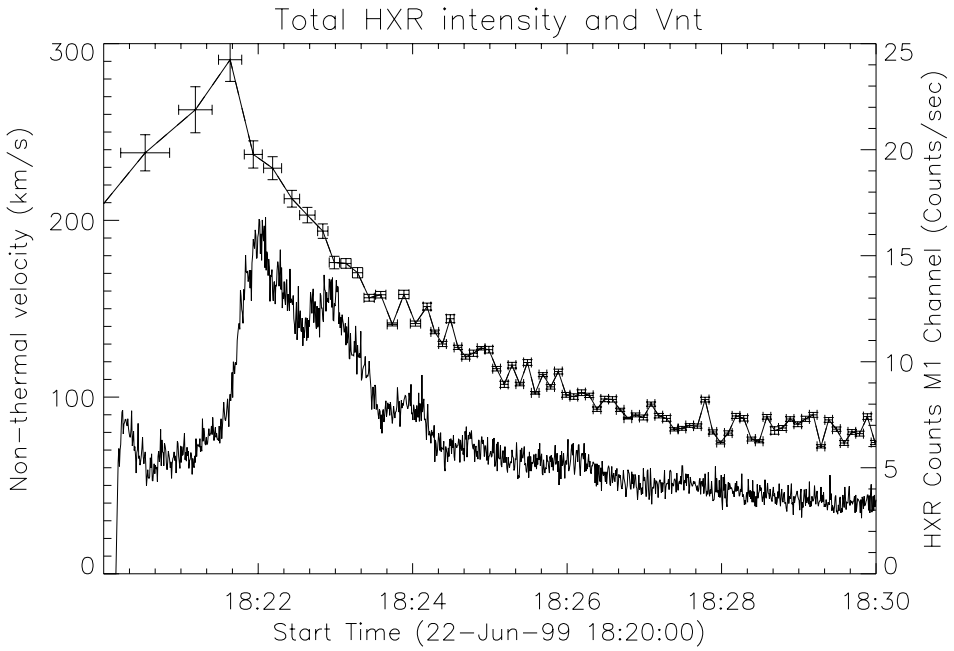

Fig. 5. The relative timings of the non-thermal broadening and HXR flux.

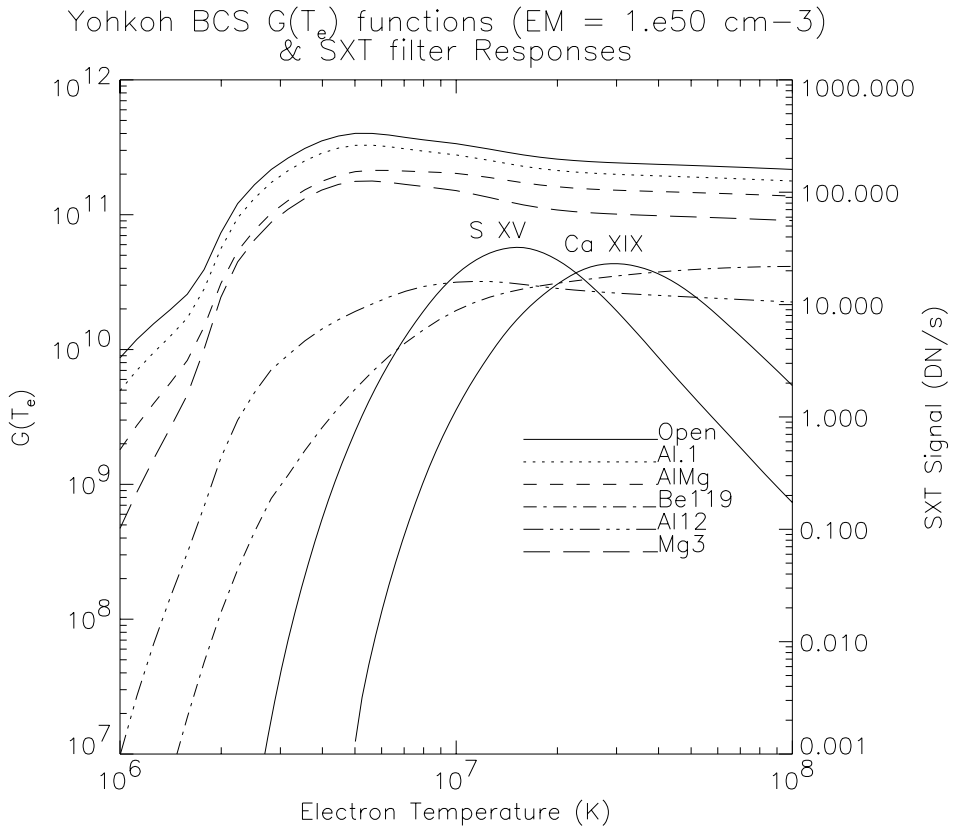

Fig. 6. The temperature responses of BCS Ca XIX channel and SXT filters.

originate from approximately the same plasma sources. By comparing TRACE 195 Å images with TRACE 171 Å(Fe IX) and 284 Å(Fe XV) we can determine which features seen in the 195 Å image are due to Fe XII and which are from Fe XXIV. This is accomplished simply by assuming that any feature that appears in Fe XII and not at either Fe XV or Fe IX must come from Fe XXIV. In Fig. 10 TRACE difference images in each EUV filter are shown along side a temperature map from SXT from the time of maximum V_{nt}. The difference images were constructed by subtracting a pre-flare image from 18:00UT. These difference images illustrate that the hot SXT component sources are co-spatial with the Fe XXIV emission in the TRACE 195 Å images. With the greater spatial resolution of TRACE we can say more accurately where, within the flare

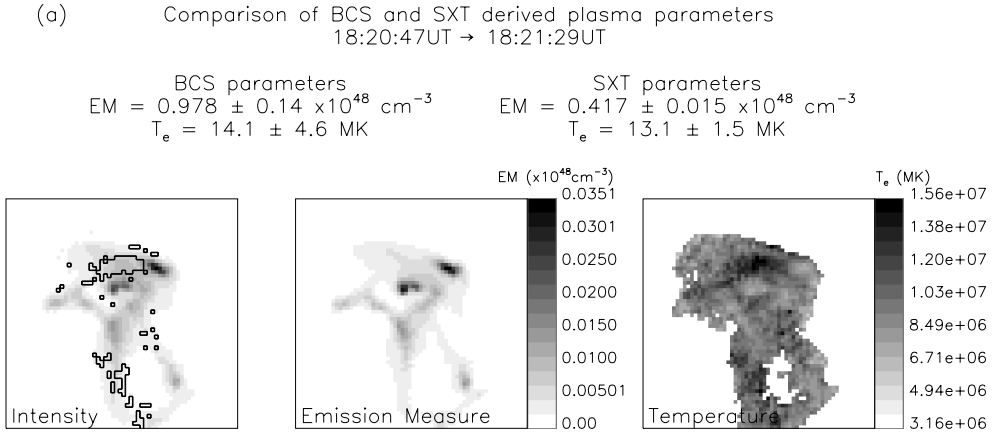

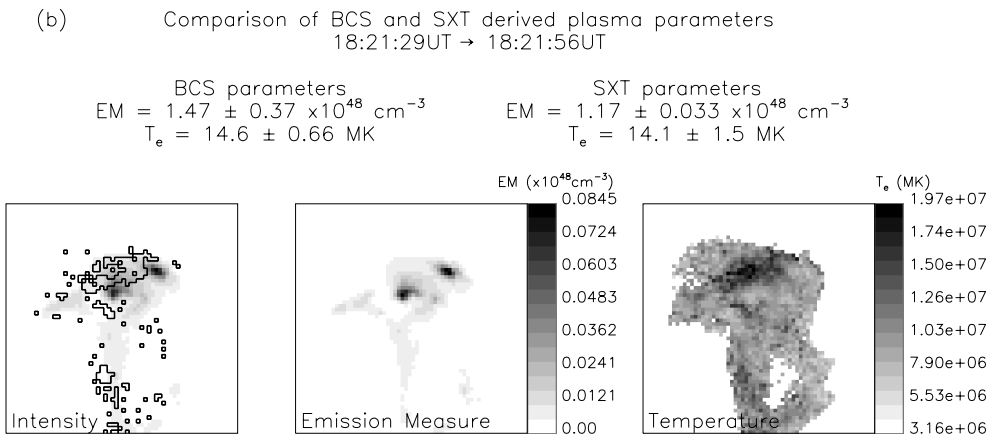

Fig. 7a and b. This figure shows an SXT intensity, EM and temperature image of the flare from **(a)** 18:20:47 → 18:21:29UT and **(b)** 18:21:29→18:21:56UT the times around the V_{nt} peak. The pixels bounded by contours have a temperature within one standard deviation of the BCS temperature for the same time interval. The large error on the BCS temperature at 18:20:47UT is due to the large non-thermal broadening which makes it difficult to obtain a good fit.

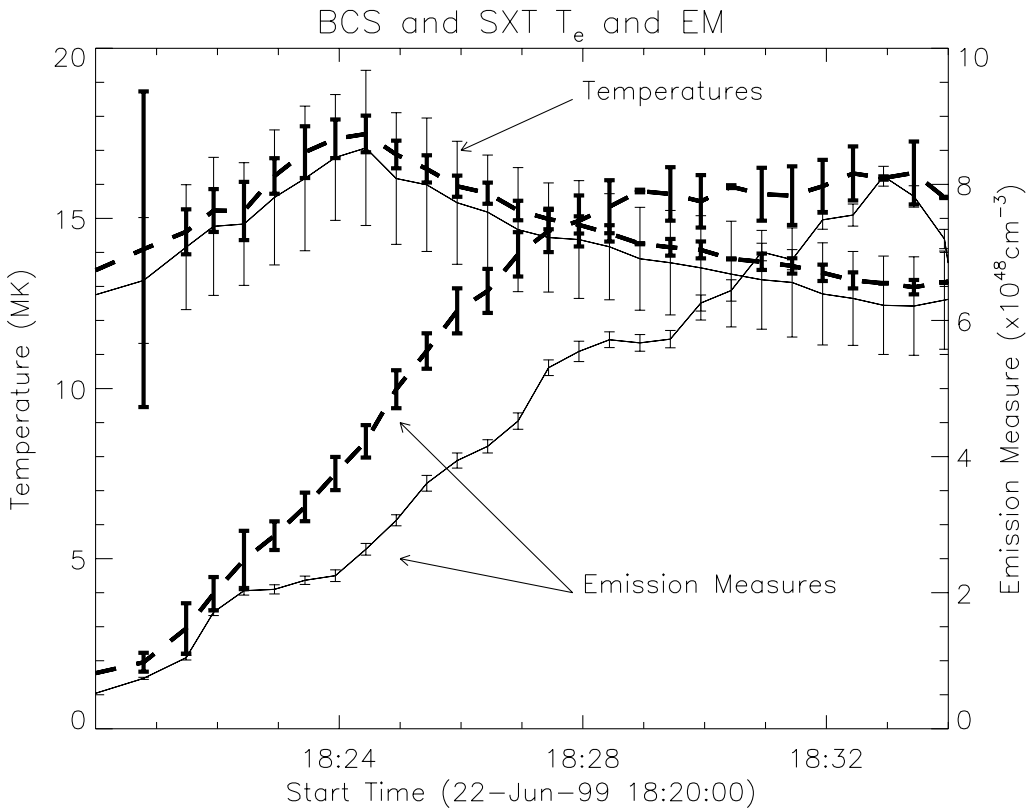

Fig. 8. The variation of temperature and emission measure with time for the SXR flare loops, from SXT (thin solid line) and BCS (thick dashed line).

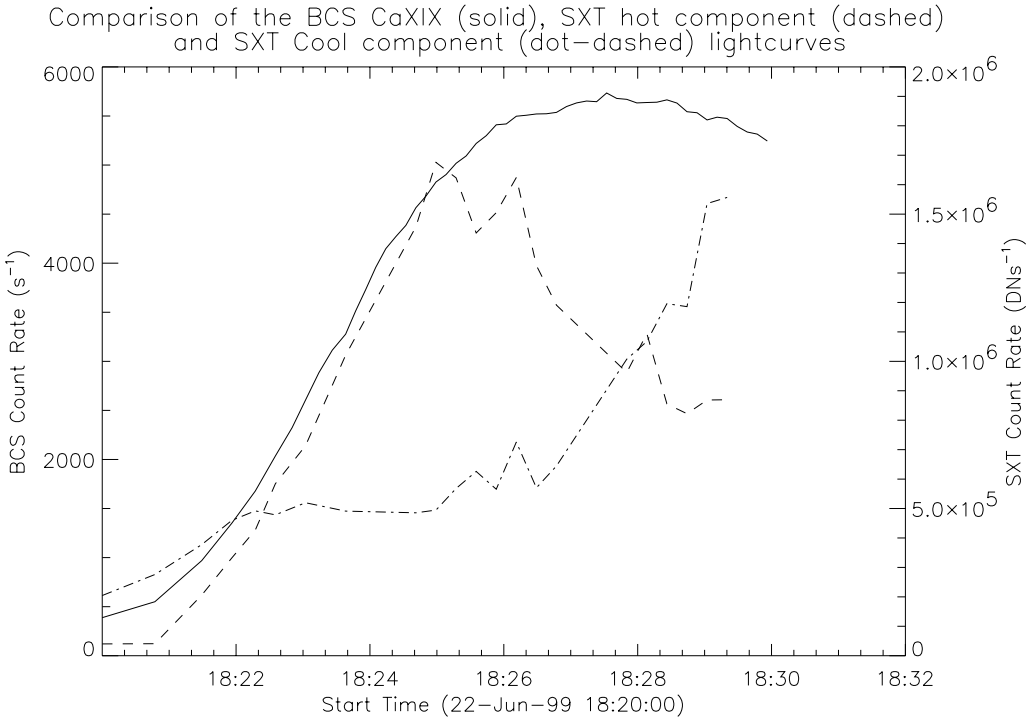

Fig. 9. Comparison of the BCS Ca XIX lightcurve (solid line) with the lightcurve of the SXT (Be199 filter) hot (dashed) and cool (dot-dashed) component.

area, this Fe XXIV emission comes from. It is slightly but significantly above the flare loops, offset to the south from the loop apex. This is co-spatial with the location of the loop top HXR source. Fig. 11 shows that the HXR loop top source is co-spatial with the hottest area of the SXT temperature map of 18:21UT and that this hot area (and HXR source, Fig. 2e) is located above the SXR loops that form during the main phase.

We have shown using BCS and SXT temperature and emission measure comparisons and TRACE Fe XXIV observations, that the dominant source of BCS Ca XIX emission at the peak value of V_{nt} is located within and above the SXR flare loops. Fig. 8 shows the variation of temperature and emission measure of the flare loops (i.e. above the footpoints). The emission measure can be seen to increase steadily as the flare progresses. Fig. 12a and b show an SXT intensity, emission measure and temperature map at later times in the flare. These figures illustrate that the area occupied by the hot plasma is expanding. Note that after 18:24UT the BCS derived emission measure becomes significantly greater than SXT, this is because the increased amounts of cooler plasma component ($\log T = 6.6 \rightarrow 6.9$) masks SXT's ability to detect the hot component (cf. Fig. 9) as discussed by Doschek (1999). Fig. 13 shows selected SXT images during the rise phase of the SXR emission. The images show that the loops are becoming brighter. We showed in Sect. 3 that this flare is a two-ribbon (CSHKP) flare, this model relies on chromospheric evaporation to create the hot SXR loops. Fig. 8 shows that the emission measure in the loops is increasing, therefore according to the model the loops are filling with SXR plasma. Unfortunately no proper motions are apparent in the SXT or TRACE images. In the TRACE images this likely results from the relatively long exposure times (6 seconds) and inadequate temporal resolution (160 seconds). In the SXT images the spatial resolution (5 arc-seconds) may be too low to observe the evaporation flows.

Chromospheric evaporation has become the generally accepted theory to explain the increase in emission measure during a flare. The evaporation of chromospheric plasma occurs as a natural physical response to the release of energy in the corona and the subsequent transport of energy down the field lines to the chromosphere. The plasma is then explosively heated to SXR temperatures and is forced up the flare loop. This process has been successfully modeled by many authors (Fisher et al. 1985a, 1985b, 1985c; Mariska et al. 1989; Yokoyama & Shibata 1998) and agrees well with the observations of SXR flares (Hori et al. 1997, 1998; Yokoyama & Shibata 1998). The CSHKP model of two-ribbon solar flares, which is believed to well describe this flare, relies on chromospheric evaporation to fill SXR loops. It has been shown that the energy spectrum of the incident electron beam onto the chromosphere affects the efficiency of converting electron energy into chromospheric evaporation. The steeper the spectrum the more input electron energy will be used to drive chromospheric evaporation rather than be radiated or conducted away from the energy deposition site (Mariska et al. 1989; Antonucci et al. 1993; McDonald et al. 1999). Fig. 14 shows the values of the photon spectral index, γ, at various times during the flare. The photon spectral index is related to the electron energy spectral index (δ), assuming thick target HXR production, by; $\gamma = \delta - 1$. The photon spectrum during the early phases of the flare 18:20:10 $\rightarrow$ 18:21:00UT is very steep, hence chromospheric evaporation will occur at this time. However we note that the value of the spectral index may be an over estimation due to contamination of the HXT LO channel by a thermal source.

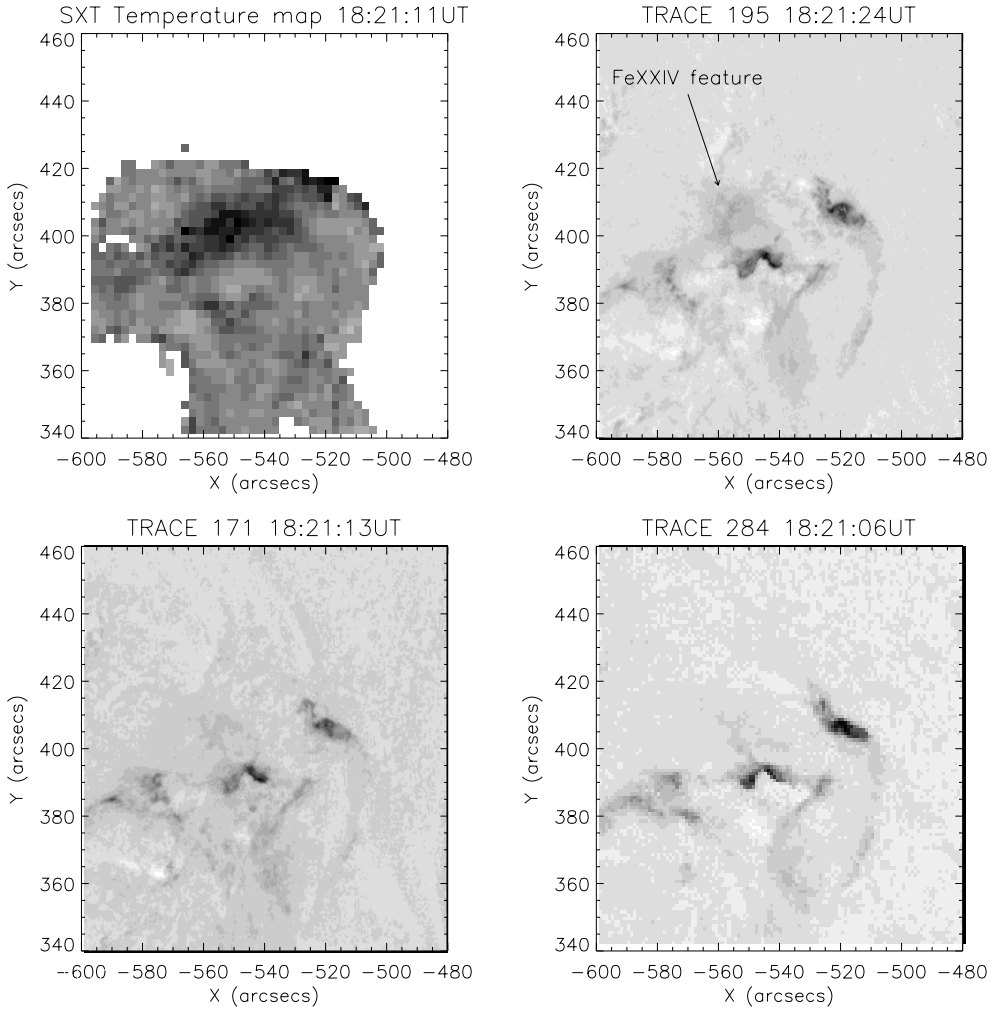

Fig. 10. TRACE difference images in all three filters and an SXT temperature image. The feature that appears in the Fe XII filter and not the other two is judged to be an Fe XXIV feature. Note that this is co-spatial with the hot component in the SXT temperature image.

The footpoint separation is $\approx 19.5 \times 10^3 km$ from TRACE Lyman α images. Assuming semicircular loops this gives a half loop length of $\approx 15 \times 10^3 km$. We assume that evaporating plasma travels up the loop at speeds ranging from a lower limit set by BCS observations of the line centroid shift ($100 kms^{-1}$) to an upper limit of the sound speed in the SXR loops. The sound speed, c_s, is given by;

$$c_s = \left(\frac{\gamma_r P}{\rho} \right)^{1/2}$$

where the pressure, $P = nkT$, the density, $\rho = nm_i$, n is the number density, k the Boltzmann constant, γ_r the ratio of specific heats and m_i the ion mass. This expression reduces to,

$$c_s = 152 T^{1/2} kms^{-1}.$$

The temperature of the flare loops is calculated from SXT observations to be $\approx 1.2 \times 10^7 K$ which gives a sound speed of $\approx 530 kms^{-1}$. Therefore the time taken for evaporating SXR plasma to reach the loop apex is $\approx 25 \rightarrow 150s$. During the early stages of evaporation the pressure in the pre-flare loop will be at its lowest level and the pressure in the evaporating plasma will be high. Therefore the up-flow velocity, driven by the pressure gradient, will be at its highest value, close to the sound speed. Hence after the start of evaporation, it will take only $\approx 25s$ for plasma to reach the flare loop apex. Therefore the small HXR burst at 18:20UT (Fig. 5) is consistent with the presence of evaporating plasma near the loop apex at 18:20:30UT.

5. Conclusions

Using the spatially resolved images of a two ribbon solar flare, from SXT, HXT and TRACE and the spectral information from BCS we have determined the location of the non-thermal soft X-ray broadenings. Using SXT and BCS temperature and emission measure comparisons and TRACE Fe XXIV observations we have shown the location of the dominant Ca XIX emission is an extended region within and above the SXR flare loops.

We therefore conclude that the source of the non-thermal line broadenings is not at the flare footpoints but a region within and above the SXR flare loops. This conclusion is in agreement with that of Khan et al. (1995) who also found that the source of the V_{nt} was not located at the flare footpoints but within the flare loops.

Having excluded the flare footpoints as a possible source of V_{nt}, there remain three alternatives: an above the loop SXR

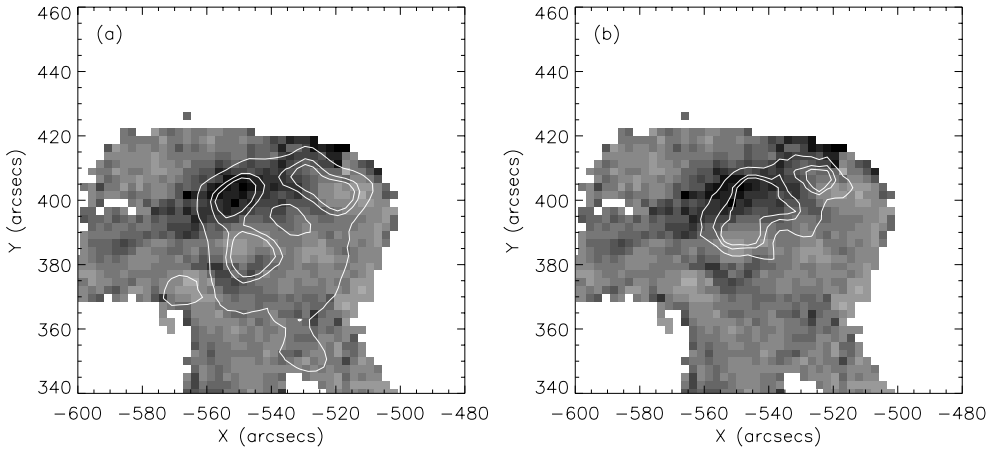

Fig. 11. a The SXT temperature image of 18:21UT with the HXT LO channel image of the same time. **b** The SXT temperature image of 18:21UT with the SXR intensity image, as contours, during the main phase (18:25UT) showing the SXR flare loops. Contour values are 30, 50 and 80% of maximum.

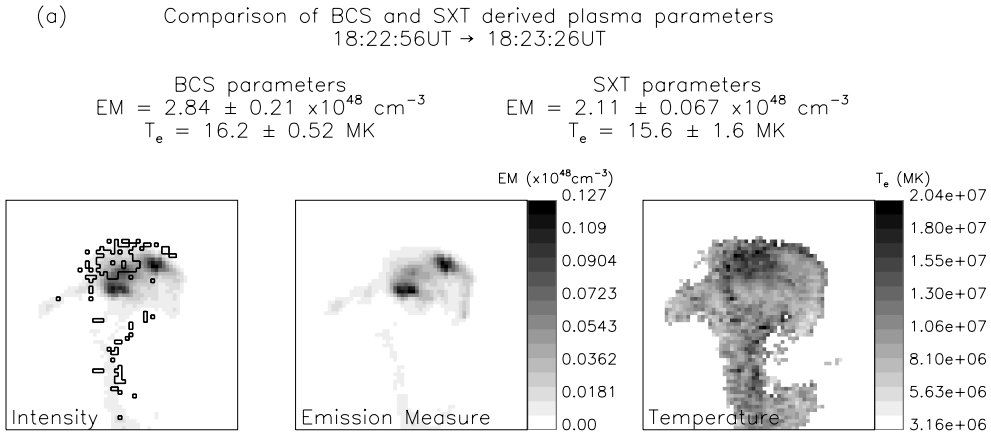

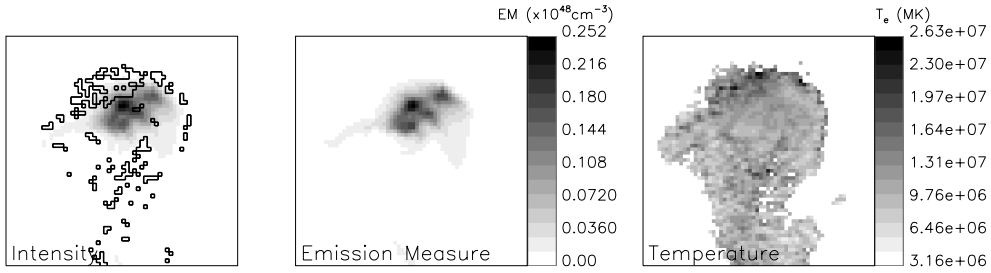

Fig. 12a and b. SXT intensity, EM and temperature images of the flare from **a** 18:22:56 → 18:23:26UT and **b** 18:26:26 → 18:26:56UT. The pixels bounded by contours have a temperature within one standard deviation of the BCS temperature for the same time interval. Note in **a** the BCS and SXT emission measure and temperature are still similar whereas in **b** the BCS and SXT emission measures now differ significantly (cf. Fig 8).

source, the SXR loop top, evaporating plasma or a combination. We do not include the reconnection site for the reasons discussed in the introduction. The evidence pertaining to each region is outlined below.

The spatial coincidence of the hottest SXR region and the HXR loop top source, both of which are above the flare loops, suggests the source of V_{nt} is also above the SXR loops, a region postulated by Tsuneta (1996, 1997) to be heated by the slow shocks extending from the reconnection region. Tsuneta et al. (1997) calculated a temperature of $\approx 20MK$ for this hot above the loop top region, using SXT, for an M2 class single loop impulsive flare. This temperature is not dissimilar to the temperature derived in this flare. This hot above the loop region could form before the start of the detectable HXR burst and hence be accountable for the increased levels of V_{nt} before the start of the HXR burst, a feature common to many flares (Alexander et al. 1998). Line of sight effects could also be significant in this flare because of its location (N20E40). If the hot SXT component was located above the SXR loops, as has been observed in other flares (Tsuneta 1996, 1997), then seen in projection it could appear to be partially located within the SXR loops.

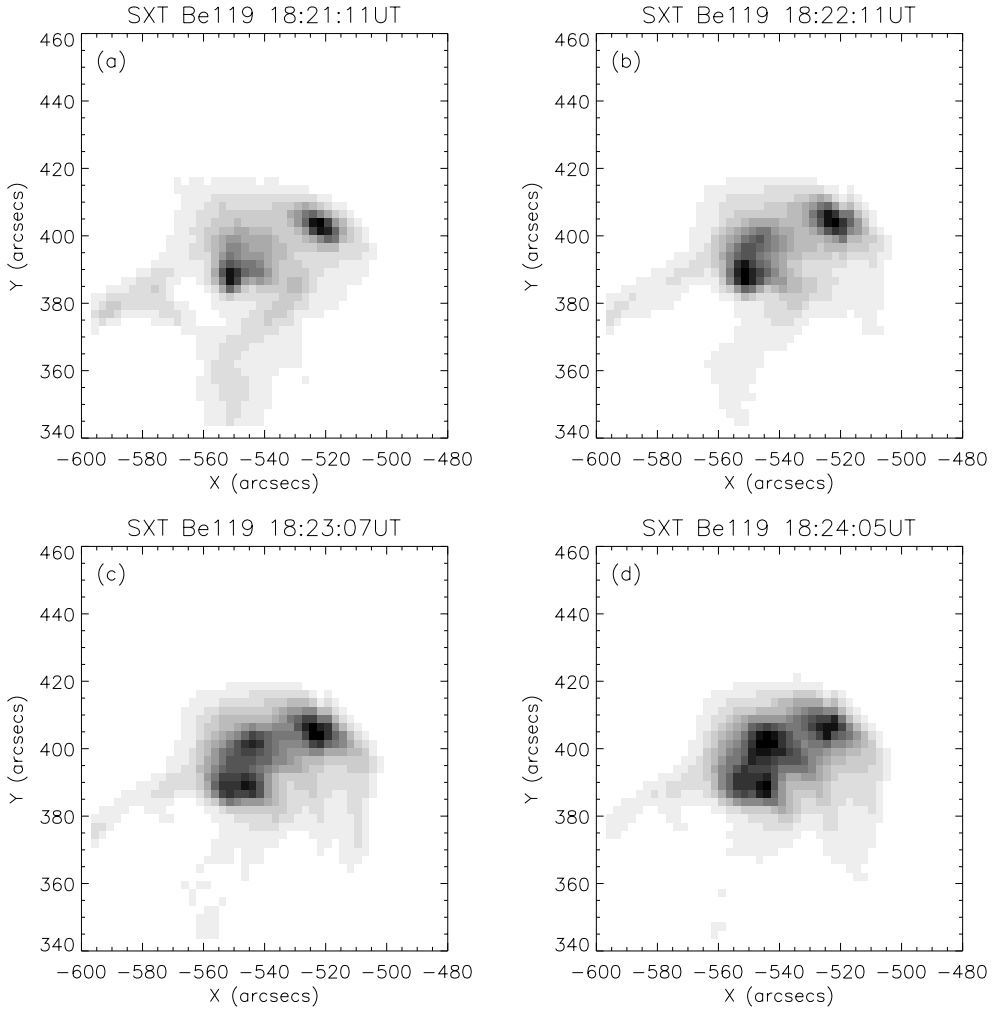

Fig. 13a–d. Selected SXT images of the flare showing the brightening of the SXR flare loops. Images are individually scaled.

In support of evaporating plasma as the source of V_{nt} is the fact that the Ca XIX source location extends over a large area that incorporates the tops of the flare loops. Also the observations of the Ca XIX line centroid shifts in the BCS data, suggesting bulk plasma motions, which change complementary to the values of V_{nt} imply a possible causal relationship. Results of recent numerical simulations of chromospheric evaporation in solar flares (Hori et al. 1997, 1998; Yokoyama & Shibata 1998) suggest that in the early phases the hot plasma is located in the upper most flare loops and is evaporating from the chromosphere. Hence the location of the Ca XIX plasma derived in this paper is in agreement with these simulations. The simulations of Hori et al. (1997) also predict temperature gradients in the loops that are in agreement with those seen in this flare. We have shown that the approximate travel time of evaporating plasma from the flare footpoints to the loop top is $\approx 25s$. The evaporating plasma is driven by the electrons producing the hard X-ray burst, therefore the elevated levels of V_{nt} after the first small HXR peak are consistent with association to evaporating plasma. We must also not rule out the presence of HXRs before they are detected by HXT if they are below the instrument detection threshold. In this case evaporation would begin earlier and further strengthen the association of V_{nt} with evaporating plasma.

The finding of Sakao (1994) that greater electron deposition and brighter HXR emission are associated with weaker magnetic field strengths has already been referred to in Sect. 3. It is thus interesting to note that the TRACE Fe XXIV observation in Fig. 10 shows that the hot SXR source is not in fact located exactly at the loop top but is slightly offset, along the loop axis, towards the south footpoint which has weaker associated magnetic field and stronger HXR emission. This image was obtained at 18:21:24 UT or very early in the HXR event when evaporating plasma might still be in the process of propagating up from the footpoints. Therefore this hot source could be evaporating plasma and is hence consistent with evaporating plasma as the source of V_{nt}. This asymmetry is also apparent in the SXT intensity images in the early stages of the flare (Fig. 13b).

We have presented arguments that the source of the V_{nt} is associated with either an above the loop top source or evaporating plasma. Both sources are consistent with the observations and we believe that neither can be excluded with the present data set. By examining a limb flare using this method it may be possible to eliminate the line of sight effects and more accurately determine the location to be either above or within the flare loops.

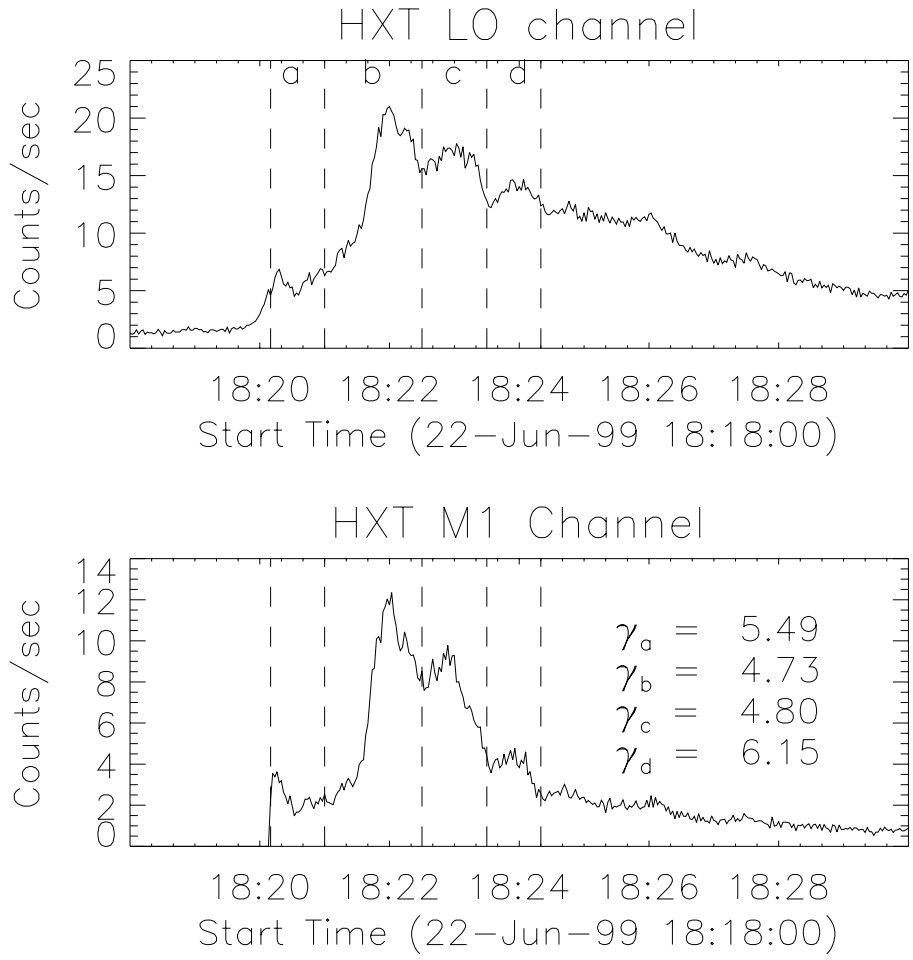

Fig. 14. The HXT LO and M1 channel flux. Vertical dotted lines indicate accumulation boundaries within which the photon spectral indices were calculated.

These results highlight the need for high spatial resolution observations of line profiles in solar flares, enabling us to obtain SXR spectra for isolated regions in the flare simultaneously, thus allowing the unambiguous determination of the source location of V_{nt}. Line profiles would be required over the whole flare area at a time resolution down to a few seconds in order to separate the pre-flare, impulsive and decay phases of the flare. Observations of transition region and chromospheric line profiles will also help in understanding the origins of V_{nt}. The Solar-B/EUV Imaging Spectrometer (EIS) scheduled for launch in 2004 will possess this capability. In the near future images from the High Energy Solar Spectroscopic Imager (HESSI) may indicate the location of hot thermal plasma in flares. These could also be used in comparison with BCS data to help locate the source of the non-thermal broadenings.

Acknowledgements. NDRR and LKH acknowledge the financial support of PPARC for a studentship and an advanced fellowship respectively.

References

Alexander D., Harra-Murnion L.K., Khan J.I., Matthews S.A., 1998, ApJ 494, L235
Antonucci E., Dodero M.A., Martin R., et al., 1993, ApJ 413, 786
Arnaud M., Rothenflug R., 1985, A&AS 60, 425
Carmichael H., 1964, In: Hess W.N. (ed.) AAS-NASA Symp., Physics of Solar Flares. NASA SP-50, Washington, DC, p. 451
Culhane J.L., Hiei E., Doschek G.A., et al., 1991, Solar Physics 136, 89
Ding M.D., Fang C., Yin S.Y., Chen P.F., 1999, A&A 348, L29
Doschek G.A., Antiochos S.K., Antonucci E., et al., 1986, In: Energetic Phenomena on the Sun. The Solar Maximum Mission Flare Workshop Proceedings, chapter 4, p. 1
Doschek G.A., Feldman, U., 1996, ApJ 459, 773
Doschek G.A., 1999, ApJ 527, 426
Fisher G.H., Canfield R.C., McClymont A.N., 1985a, 289, 414
Fisher G.H., Canfield R.C., McClymont A.N., 1985b, 289, 425
Fisher G.H., Canfield R.C., McClymont A.N., 1985c, 289, 434
Feldman U., Laming J.M., Doschek G.A., et al., 1999, ApJ 505, L418
Fletcher L., Martens P.C.H., 1998, ApJ 505, 418
Fletcher L., 1999, Magnetic Fields and Solar Processes. The 9^{th} European Meeting on Solar Physics, University of Florence, Italy, 693
Fludra A., Lemen J.R., Jakimiec J., et al., 1989, ApJ 344, 991
Handy B.N., Acton L.W., Kankelborg C.C., et al., 1999, Solar Physics 187, 229
Harra-Murnion L.K., Akita K., Watanabe T., 1997, ApJ 479, 464
Hirayama T., 1974, Solar Physics 34, 323
Hori K., Yokoyama T., Kosugi T., Shibata K., 1997, ApJ 589, 426
Hori K., Yokoyama T., Kosugi T., Shibata K., 1998, ApJ 500, 492
Jakimiec J., Tomczak M., Falewicz R., et al., 1998, A&A 334, 1112

Khan J.I., Harra-Murnion L.K., Hudson H.S., et al., 1995, ApJ 452, L153
Kopp R.A., Pneuman, G.W., 1976, Solar Physics 50, 85
Kosugi T., Makishima K., Murakami T., et al., 1991, Solar Physics 136, 17
Lang J., Brown C.M., Magraw J.E., Payne, J., 1993, The Laboratory Calibration of the *Yohkoh* Bragg Crystal Spectrometer. Rutherford Appleton Laboratory, Didcot
Mariska J.T., Emslie G.A., Li P., 1989, ApJ 341, 1067
Mariska J.T., Doschek G.A., Bentley R.D., 1993, ApJ 419, 418
Mariska J.T., Sakao T., Bentley R.D., 1996, ApJ 459, 815
Mariska J.T., McTiernan J.M., 1999, ApJ 514, 484
Masuda S., 1994, Ph.D. Thesis, University of Tokyo
McDonald L., Harra-Murnion L.K., Culhane J.L., 1999, Solar Physics 185, 323
Metcalf T., Alexander D., 1999, ApJ 522, 1108
Mewe R., Lemen J.R., Peres G., et al., 1985, A&A 152, 229
Miller J.A., Cargill P.J., Emslie A.G., et al., 1997, JGR 102, 14, 631
Sakao T., 1994, Ph.D. Thesis, Univ. Tokyo
Schrijver C.J., Title A.M., Berger T.E., et al., 1999, Solar Physics 187, 261
Shibata K., 1999, In: Bastian T., Gopalswamy N., Shibasaki K. (eds.) Solar Physics with Radio Observations. Proc. Nobeyama Symposium, Kiyosato, Japan
Somov B., Litvinenko Y.E., Kosugi T., et al., 1999, Magnetic Fields and Solar Processes. The 9^{th} European Meeting on Solar Physics, University of Florence, Italy, 701
Sturrock P.A., 1966, Nat 211, 695
Tsuneta S., Acton L., Bruner M., et al., 1991, Solar Physics 136, 37
Tsuneta S., 1996, ApJ 456, 840
Tsuneta S., Masuda S., Kosugi T., Sato J., 1997, ApJ 478, 787
Tsuneta S., Naito 1998, ApJ 495, L67
Warren H., Bookbinder J.A., Forbes T.G., et al., 1999, ApJ 527, L121
Warren H.P., 2000, ApJ 536, L105
Wheatland M.S., Melrose D.B., 1995, Solar Physics 185, 283
Wülser J-P. Canfield R.C., Acton L.W., et al., 1994, ApJ 424, 459
Yokoyama T., Shibata K., 1998, ApJ 494, L113
Yokoyama T., Akita K., Morimoto T., et al., 2000, submitted ApJ